Journal of Quantitative Spectroscopy & Radiative Transfer 233 (2019) 134–148

Contents lists available at ScienceDirect

Journal of Quantitative Spectroscopy & Radiative Transfer

journal homepage: www.elsevier.com/locate/jqsrt

Assessing turbulence-radiation interactions in turbulent flows of non-gray media

S. Silvestri*, D.J.E.M. Roekaerts, R. Pecnik

Process and Energy Department, Delft University of Technology, Delft, The Netherlands

ARTICLE INFO

Article history:
Received 30 September 2018
Revised 16 May 2019
Accepted 19 May 2019
Available online 21 May 2019

Keywords:
Turbulence
Direct numerical simulation
Turbulence radiation interactions

ABSTRACT

The present work investigates gray and non-gray gas turbulence-radiation interactions (TRI) in a turbulent channel flow bounded by two isothermal hot and cold walls. Cases of various optical thicknesses are examined using Direct Numerical Simulations (DNS), coupled with a computationally efficient Monte Carlo radiative transfer solver. Several novel concepts are presented which not only allow to uniquely characterize but also to accurately model TRI for a wide range optical properties in non-reacting flows. First, we propose linear relations between fluctuations in radiative quantities (emission, incident radiation and absorption coefficient) and temperature fluctuations, where the coefficients of proportionality are solely functions of averaged quantities (e.g. emission fluctuations E' can be related with temperature θ in the following way, $E' = f_E(\bar{\theta})\theta'$). The validity of these linear relations is supported by an excellent agreement with DNS for all considered gray gas cases. Using these linear relations it is possible to show that gray gas TRI can be fully characterized without accounting for fluctuations in absorption coefficient. Second, TRI for non-gray gases is investigated and the developed concepts are extended to account for the spectrally varying absorption coefficient. In particular, the derived linear relations are used to show that the influence of a wavelength dependent κ manifests itself in an increase of the "effective" optical thickness of the flow. A new turbulence based spectral averaging is proposed that results in a mean κ, which uniquely characterizes TRI of non-gray participating media. Finally, we apply our models to estimate classical TRI (impact of fluctuations in radiative quantities on the mean radiative source) and a perfect agreement with DNS is observed. We anticipate that the proposed formulations also have the potential to allow for a better characterization in TRI, where strong temperature fluctuations are present, such as in combustion applications. Yet, this needs to be explored in future studies.

1. Introduction

When dealing with high temperature applications, radiation is the most significant mode of heat transfer. Therefore, it is important to understand the coupling of three heat transfer modes in high temperature radiative flows. Several numerical studies and experimental investigations have observed the appearance of interactions between the turbulent temperature field (i.e., the fluctuations of temperature and internal energy) and radiation in turbulent flows of participating media, which cause strong heat transfer modifications [1]. These interactions lead to the appearance of a fluctuating radiative field, which in turn acts as source/sink for quantities such as temperature variance and turbulent heat transfer. As a consequence, two distinct but interrelated aspects of turbulence radiation interactions (TRI) are of importance. Namely, the influence of the turbulent temperature field in the modification of radiative quantities, and the effect of radiative heat transfer on temperature statistics.

1.1. Previous works

Most of the studies deal with the first aspect, particularly in reactive flows, where, due to the high levels of temperature fluctuations, $\overline{T^4} \neq \overline{T}^4$. This causes a disagreement between the radiative quantities calculated with the mean and the instantaneous temperature which can be as high as 30% as demonstrated in the work of Coelho et al. [2]. In their 2009 study, Gupta et al. [3] examined the impact of TRI in a gray turbulent planar channel flow through the aid of large eddy simulation (LES). They investigated both reactive and non reactive flows. In the latter case they noticed that, while mean profiles are significantly affected by radiative heat transfer, TRI impact proved to be minimal and safely negligible. It

* Corresponding author.
E-mail addresses: s.silvestri@tudelft.nl (S. Silvestri), r.pecnik@tudelft.nl (R. Pecnik).

https://doi.org/10.1016/j.jqsrt.2019.05.018
0022-4073/

is important to remind that, in their paper, they define TRI only as the influence of turbulence on the averaged radiative transfer equation (RTE), i.e. the magnitude of $\overline{T^4}/\overline{T}^4$ and $\overline{\kappa_p T^4}/(\overline{\kappa}_p \cdot \overline{T^4})$. The impact of radiative fluctuations on mean and rms temperature profiles was not assessed. On the other hand, the same ratios grow drastically for a reactive flow reaching values of 3 to 6 near the flame front [3]. Deshmukh et al. [4] assessed the influence of TRI in statistically one-dimensional premixed flame using a fictitious composition dependent gray gas mimicking hydrogen-air combustion products. They estimated the impact of both emission and absorption TRI by calculating absorption coefficient–blackbody intensity correlation factor and absorption coefficient–incident radiation correlation factor for two different optical thickness values (1 and 10). While the first one was always relevant, they showed that the second correlation factor increases to a significant value only at a larger optical thickness. Moreover, Tesse et al. [5] modeled radiative transfer in a sooty turbulent ethylene-air diffusion jet flame. Their results confirm the findings of Ref. [2] by identifying an additional radiative heat loss of around 30% due to the TRI mechanism. Again, by TRI only the effect of turbulence on the RTE was intended. They also pinpointed the major role of soot in the heat release due to radiation. Finally, Roger et al. [6] evaluated the magnitude of sub-grid scale TRI (on a LES grid) in a turbulent non reactive plane jet. They noticed that sub-grid scales are not significant near the jet edges, where radiative heat transfer peaks. Therefore, they state that for this configuration TRI sub-grid scales can be neglected.

More recently, the influence of radiative heat transfer on the turbulent temperature field has been investigated with the aid of DNS and LES in different conditions. Sakurai et al. [7] examined the role of radiation in the modification of convective heat transfer in a horizontally buoyant gray turbulent channel flow. They noticed that, since radiative heat transfer acts as a sink of temperature fluctuations, organized large scale vortices characteristic of mixed convection are disrupted, making the system more similar to a forced convection case. The optical depths investigated were limited to $\tau = 0.1$ due to the optically thin approximation employed. Nevertheless, they noticed a reduction of turbulent heat transfer with the increase of τ. On the other hand, they explained these results with the modification of mean temperature gradient (due to the action of an averaged radiative source) rather than through the direct dissipative action of radiative emission. The same reduction in temperature variance and turbulent heat flux was observed by Vicquelin et al. [8] in their study from 2014. They coupled a variable density DNS to an accurate spectral Monte Carlo radiative solver to study the effect of radiation on turbulence with varying temperature and Reynolds number. After investigating radiative effects on the mean temperature profile [9], they analyzed the modification of turbulent heat flux and enthalpy budgets and proposed a radiative scaling to collapse turbulent quantities to universal profiles accounting for radiative heat transfer. Moreover, Ghosh et al. [10] extended the study of TRI to gray supersonic flows. They employed LES coupled to a discrete ordinate method (DOM) to investigate mean quantities and energy budgets for turbulent channel and pipe flows. Once again, their results report a growth of TRI impact with an optical thickness increase, although the range of investigated τ remained in the optically thin region. Furthermore, the same group published a study in 2015 [11] on the effect of radiative heat transfer in both inert and reacting mixing layers. Again, a combination of gray gas DOM and LES was used to solve the governing equations. They focussed on the modification of thermodynamic variables fluctuations in the presence of a radiative field. In particular, they report a decrease in temperature and density fluctuations by the action of radiative transfer for a reacting mixing layer, while the same quantities exhibit an increase in an inert mixing layer. While in the first case the direct action of radiation on the temperature variance transport equation is deemed to be the cause, in the second case the increased fluctuations are explained by the increase in the production term (in the same transport equation) due to indirect radiation effects. Finally, in our recent DNS study [12] we analyzed the effects of radiative heat transfer on temperature structures in a fully developed turbulent channel flow. We used the gray gas approximation and a constant κ to show the influence of optical thickness (τ) in the modification of the turbulent temperature field. The results showed that, not only the magnitude of TRI changes drastically upon increasing τ, but also the behaviour of the TRI changes due to the shortening of radiative length scales. If τ is sufficiently low, Radiative power fluctuations (Q_r'), which tend to reduce temperature variance, are completely described by emission fluctuations. On the other hand, for a large enough τ, also incident radiation fluctuations play a role by inducing a recovery in the fluctuations of the turbulent temperature field. In particular, this recovery is affected by the dimension of the temperature scales, since larger structures are more efficient in retaining the emitted radiation. In addition, the anisotropy of temperature scales delays the recovery due to the larger surface to volume ratio when compared to the isotropic nature of radiative emission.

1.2. Scope of this research

TRI is highly non-linear and hard to predict due to the counter intuitive dependency on the absorption coefficient. Consequently, TRI has not been fully characterized, particularly for complex problems involving non-gray radiative heat transfer. Traditionally, modeling efforts directed towards TRI have accounted for the full radiative source. Based on the results of our previous work [12], we highlight the necessity of separately accounting for emission and absorption. The scope of this paper is, therefore, to provide a universal understanding of TRI, especially in the framework of the development of radiative field fluctuations. To achieve this objective, linear relations for the radiative fluctuations are formulated by analytical derivation. These relations provide a key to successfully understand and model TRI in non-reactive turbulent flows for the considered optical thickness range. Furthermore, the effect of a variable absorption coefficient, decomposed in a mean and fluctuating part, is investigated to demonstrate that TRI is fully accounted for by considering the variations of the mean absorption coefficient only. Finally, the impact of a spectrally varying absorption coefficient is examined thoroughly.

2. Governing equations

The governing equations for a variable density absorbing-emitting turbulent flow are displayed below. We employed a low-Mach number approximation of the Navier–Stokes equations, which neglects the presence of an acoustic field. The asterisk * stands for dimensional variables, while variables without asterisk represent non-dimensional quantities. The Navier–Stokes equations are given by

$$\frac{\partial \rho}{\partial t} + \frac{\partial \rho u_j}{\partial x_j} = 0, \tag{1}$$

$$\frac{\partial \rho u_i}{\partial t} + \frac{\partial \rho u_i u_j}{\partial x_j} = -\frac{\partial p}{\partial x_i} + \frac{\partial \tau_{ij}}{\partial x_j}, \tag{2}$$

$$\frac{\partial \rho \theta}{\partial t} + \frac{\partial \rho u_j \theta}{\partial x_j} = \frac{1}{RePr}\frac{\partial^2 \theta}{\partial {x_j}^2} - \frac{Q_r}{RePrPl}, \tag{3}$$

where

$$\tau_{ij} = \frac{1}{Re}\left(\frac{\partial u_i}{\partial x_j} + \frac{\partial u_j}{\partial x_i} - \frac{2}{3}\frac{\partial u_k}{\partial x_k}\delta_{ij}\right), \text{ and } \rho = \frac{T_0}{T_0 + \theta}. \tag{4}$$

Note that thermal conductivity, k^*, specific heat capacity, c_p^*, and viscosity, μ^*, are considered constant and have been incorporated in the definitions of *Re* and *Pr*. Scattering has been neglected. The spectral intensity I_λ satisfies the radiative transfer equation (RTE), given as

$$s_j \frac{\partial I_\lambda}{\partial x_j} = \kappa_\lambda (I_{b\lambda} - I_\lambda). \tag{5}$$

The radiative power source is calculated as

$$Q_r = \int_0^\infty \kappa_\lambda \left(4I_{b\lambda} - \frac{1}{\pi}\int_{4\pi} I_\lambda d\Omega\right) d\lambda. \tag{6}$$

The non-dimensional variables are defined as

$$\boldsymbol{x} = \frac{\boldsymbol{x}^*}{\delta^*}, \quad t = t^* \frac{U_b^*}{\delta^*}, \quad \boldsymbol{u} = \frac{\boldsymbol{u}^*}{U_b^*}, \quad p = \frac{p^*}{\rho_c^* U_b^{*2}}, \quad \theta = \frac{T^* - T_c^*}{T_h^* - T_c^*},$$

$$I_{b\lambda} = \frac{I_{b\lambda}^* \pi}{\sigma^* T_c^{*4}}, \quad I_\lambda = \frac{I_\lambda^* \pi}{\sigma^* T_c^{*4}}, \quad \kappa_\lambda = \delta^* \kappa_\lambda^*,$$

where $\boldsymbol{x}$, t, $\boldsymbol{u}$, p, θ, ρ, $I_{b,\lambda}$, I_λ and κ_λ are non-dimensional space coordinates, time, pressure, temperature, density, blackbody intensity, intensity and absorption coefficient, respectively. The non-dimensional parameters Reynolds, Prandtl, Planck number and T_0, which are kept constant among all cases, are defined as

$$Re = \frac{U_b^* \delta^* \rho_c^*}{\mu^*} = 3750, \quad Pr = \frac{\mu^* c_p^*}{k^*} = 1, \quad Pl = \frac{k^* \Delta T^*}{\sigma^* T_c^{*4} \delta^*} = 0.03,$$

$$T_0 = \frac{T_c^*}{\Delta T^*} = 1.5, \tag{7}$$

where $U_b^*, \delta^* \rho_c^*$, σ^*, T_c^*, T_h^* and ΔT^* are bulk velocity, half channel height, cold wall density, Stefan–Boltzmann constant, cold and hot wall temperature and their difference, respectively. The radiative power, equation (6), can be rewritten to highlight the radiative quantities of interest as

$$Q_r = \kappa_p (E - G), \tag{8}$$

where κ_p, E and G are Plank-mean absorption coefficient, emission and reference incident radiation (from now on referred to just as incident radiation), defined as

$$\kappa_p = \frac{1}{\int_0^\infty I_{b,\lambda} d\lambda} \int_0^\infty \kappa_\lambda I_{b,\lambda} d\lambda, \tag{9}$$

$$E = 4\left(\frac{\theta}{T_0} + 1\right)^4, \tag{10}$$

$$G = \frac{1}{\kappa_p \pi} \int_0^\infty \kappa_\lambda \int_{4\pi} I_\lambda d\Omega d\lambda. \tag{11}$$

For gray gas cases, $\kappa^*(\theta) = C_\kappa \mathcal{P}(T^{*-1})$ where $\mathcal{P}$ is a fifth order polynomial which approximates the Planck-mean absorption coefficient of water vapour in the range of 300–2500 K [13]. The coefficients $c_0 - c_5$ are multiplied by a pre-factor C_κ to achieve the desired optical thickness as done in Refs. [3,7].

$$\kappa = \delta^* \left(c_0 + \frac{c_1}{T} + \frac{c_2}{T^2} + \frac{c_3}{T^3} + \frac{c_4}{T^4} + \frac{c_5}{T^5}\right). \tag{12}$$

In case of a gray gas approximation, G coincides with the exact definition of incident radiation. While gray gas cases will be unambiguously compared using optical thickness based on mean absorption coefficient

$$\tau = \frac{1}{2}\int_0^2 \overline{\kappa} dy, \tag{13}$$

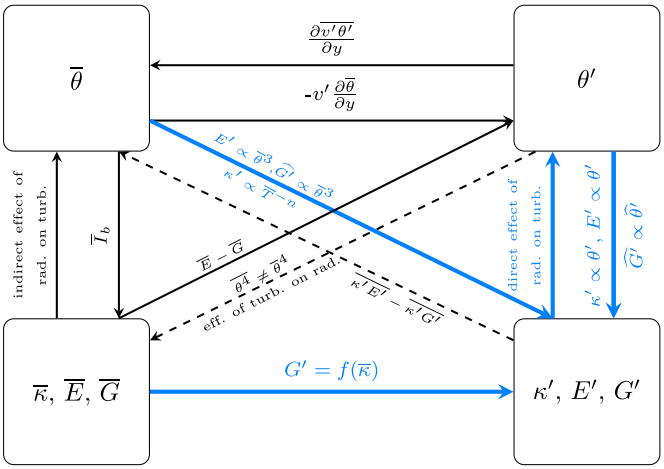

Fig. 1. Schematic representing the TRI pathways and the connections between the quantities involved.

non-gray cases will be compared using both Planck-mean optical thickness (τ)

$$\tau = \frac{1}{2}\int_0^2 \overline{\kappa}_p dy, \tag{14}$$

and global transmissivity (t), defined as

$$t = \frac{1}{I_b(\overline{T}|_{y=1})} \int_0^\infty I_{b\lambda}(\overline{T}|_{y=1}) \exp\left(-\kappa_\lambda(\overline{T}|_{y=1})\right) d\lambda. \tag{15}$$

3. Overview of turbulence-radiation interactions

Fig. 1 shows a schematic which describes all the interaction pathways between the mean and the fluctuating temperature field, and the radiative quantities. The two dashed lines show pathways that, in non-reactive flows, are negligible with respect to the other coupling phenomena. The first pathway ($\theta' \rightarrow \overline{\kappa}, \overline{E}, \overline{G}$) indicates the impact of a fluctuating temperature field θ' on the mean radiative quantities $\overline{\kappa}$, $\overline{E}$ and $\overline{G}$. In non-reactive flows, this path is negligible since $T^{*\prime}/\overline{T^*} \ll 1$ (weak temperature fluctuations) as reported in several previous works [3,6,8,10]. The second pathway ($\kappa', E', G' \rightarrow \overline{\theta}$) represents the direct impact of radiative fluctuations on the mean temperature. This path is much smaller than its counterpart (the effect of average radiative quantities on the average temperature, $\overline{\kappa}, \overline{E}, \overline{G} \rightarrow \overline{\theta}$), but despite small, it is the most investigated in previous research on TRI. We will shortly address this path at the end of this paper (Section 9) and show that the framework developed here can also be used to model these classical TRI relations.

The largest effect of radiative fluctuations on $\overline{\theta}$ is due to the modification of θ' and the consequent change in turbulent heat transfer ($\overline{\theta} \rightarrow \kappa', E', G' \leftrightarrow \theta' \rightarrow \overline{\theta}$). In non-reactive flows, this mechanism is the dominant TRI effect and is thus the focus of this work. In order to quantify and model this TRI mechanism, it is necessary to provide approximations for the fluctuations of radiative quantities depicted in the bottom right block of Fig. 1. For this reason, the next sections will focus on investigating and modeling the paths highlighted in blue in Fig. 1.

4. Approximating radiative field fluctuations

TRI manifests in the appearance of a fluctuating radiative field. As such, in this section, we will derive mathematical relations to express the fluctuations of radiative quantities. We will test these relations in the following sections using DNS data to prove the validity of the assumptions employed. Referring to Eq. (8) and the

bottom left box in Fig. 1, the quantities that require estimation are

$$E' \quad \kappa' \quad G'. \tag{16}$$

The above κ is the same absorption coefficient found in both Eqs. (5) and (8) for a gray gas case, while it coincides with the Planck-mean absorption coefficient, Eq. (9), for non-gray gasses. The proposed linear relations take the following form

$$E' \approx f_E\theta' \quad \kappa' \approx f_\kappa\theta' \quad G' \approx f_G\theta', \tag{17}$$

where the coefficients of proportionality f_κ, f_E and f_G only depend on mean quantities and are independent of θ'.

4.1. Approximating E′

Given Eq. (10), emission fluctuations are defined as

$$E' = E - \overline{E} = 4\left(\frac{\theta}{T_0}+1\right)^4 - \overline{4\left(\frac{\theta}{T_0}+1\right)^4}. \tag{18}$$

By substituting the definition of the Reynolds decomposition of $\theta = \theta' + \overline{\theta}$ and rearranging the terms with the same order of θ', it is possible to obtain

$$\begin{aligned} E' = &\left(\frac{16\overline{\theta}^3}{T_0^4}+\frac{48\overline{\theta}^2}{T_0^3}+\frac{48\overline{\theta}}{T_0^2}+\frac{16}{T_0}\right)\theta' \\ &+\left(\frac{24\overline{\theta}^2}{T_0^4}+\frac{48\overline{\theta}}{T_0^3}+\frac{24}{T_0^2}\right)(\theta'^2-\overline{\theta'^2}) \\ &+\left(\frac{16\overline{\theta}}{T_0^4}+\frac{16}{T_0^3}\right)(\theta'^3-\overline{\theta'^3}) \\ &+\left(\frac{4}{T_0^4}\right)(\theta'^4-\overline{\theta'^4}). \end{aligned} \tag{19}$$

Considering only the first order terms, θ', the first coefficient of proportionality f_E is defined as

$$f_E = \frac{16\overline{\theta}^3}{T_0^4}+\frac{48\overline{\theta}^2}{T_0^3}+\frac{48\overline{\theta}}{T_0^2}+\frac{16}{T_0}. \tag{20}$$

4.2. Approximating κ′

In order to derive f_κ, we will use the dimensional temperature T^*, with its mean $\overline{T^*} = T_c^* + \overline{\theta}\Delta T^*$ and its fluctuation as $T^{*\prime} = \theta'\Delta T^*$. The asterisk will be dropped hereafter for the sake of simplicity. While for the gray gas cases, κ is exactly a 5th order polynomial of T^{*-1}, for the non-gray gas cases the coefficients $c_0 - c_5$ are found by fitting κ_p^* using a 5th order polynomial, such that for all cases

$$\overline{\kappa} = \delta^*\left(c_0 + \overline{\left(\frac{c_1}{T}\right)} + \overline{\left(\frac{c_2}{T^2}\right)} + \overline{\left(\frac{c_3}{T^3}\right)} + \overline{\left(\frac{c_4}{T^4}\right)} + \overline{\left(\frac{c_5}{T^5}\right)}\right). \tag{21}$$

By assuming low temperature fluctuations, $T'/\overline{T} \ll 1$ (invalid for reactive flows), and by performing a Taylor expansion (neglecting higher order terms), it is possible to show that $\overline{1/T^\alpha} \approx 1/\overline{T}^\alpha$. Therefore, Eq. (21) can be approximated as

$$\overline{\kappa} \approx \delta^*\left(c_0 + \frac{c_1}{\overline{T}} + \frac{c_2}{\overline{T}^2} + \frac{c_3}{\overline{T}^3} + \frac{c_4}{\overline{T}^4} + \frac{c_5}{\overline{T}^5}\right). \tag{22}$$

Using the Reynolds decomposition for $\kappa' = \kappa - \overline{\kappa}$, it is possible to approximate κ' using (22). Starting with the terms containing T^{-1}, one obtains, by assuming that $T'\overline{T} \ll \overline{T}^2$,

$$c_1\left(\frac{1}{T}-\frac{1}{\overline{T}}\right) = c_1\left(\frac{\overline{T}-T}{T\overline{T}}\right) \approx -c_1\frac{T'}{\overline{T}^2} = -c_1\frac{\Delta T}{\overline{T}^2}\theta'. \tag{23}$$

Accordingly, the terms with T^{-2} can be expressed as

$$c_2\left(\frac{1}{T^2}-\frac{1}{\overline{T}^2}\right) = c_2\left(\frac{\overline{T'^2}-2\overline{T}T'-T'^2}{(\overline{T}^2+2\overline{T}T'+T'^2)(\overline{T}^2+\overline{T'^2})}\right). \tag{24}$$

Again, neglecting smaller terms in both the denominator ($\approx \overline{T}^4$) and the numerator ($2\overline{T}T' \gg \overline{T'^2} - T'^2$) yields

$$c_2\left(\frac{1}{T^2}-\frac{1}{\overline{T}^2}\right) \approx -c_2\frac{2\Delta T}{\overline{T}^3}\theta'. \tag{25}$$

In the same fashion, it is possible to demonstrate that

$$\begin{aligned} c_3\left(\frac{1}{T^3}-\frac{1}{\overline{T}^3}\right) &\approx -c_3\frac{3\Delta T}{\overline{T}^4}\theta', \\ c_4\left(\frac{1}{T^4}-\frac{1}{\overline{T}^4}\right) &\approx -c_4\frac{4\Delta T}{\overline{T}^5}\theta', \\ c_5\left(\frac{1}{T^5}-\frac{1}{\overline{T}^5}\right) &\approx -c_5\frac{5\Delta T}{\overline{T}^6}\theta'. \end{aligned} \tag{26}$$

Combining the above expressions, the second function is given by

$$f_\kappa = -\delta^*\left(c_1\frac{\Delta T}{\overline{T}^2}+c_2\frac{2\Delta T}{\overline{T}^3}+c_3\frac{3\Delta T}{\overline{T}^4}+c_4\frac{4\Delta T}{\overline{T}^5}+c_5\frac{5\Delta T}{\overline{T}^6}\right). \tag{27}$$

4.3. Approximating G′

Owing to the non-local nature of incident radiation G, it is convenient to express its relation with the temperature field in the wavenumber domain (i.e., Fourier transformed), rather than in the spatial domain. A similar approach has been used by Soufiani [14] and in our previous work [12], in case of a uniform κ, to visualize the influence of radiative heat transfer on the turbulent temperature spectrum. For the sake of simplicity, it is useful to first assume isotropic turbulence and then to generalize the relations for anisotropic cases. The derivation will be performed for a gray gas, and the extension for non-gray gases will follow in Section 8.2. In the case of homogeneous isotropic turbulence with a gray gas, the Fourier transform of incident radiation fluctuations simply yields

$$\widehat{G'}(\boldsymbol{\omega}) = \frac{1}{\pi}\int_{4\pi}\widehat{I'}(\boldsymbol{\omega})d\Omega, \tag{28}$$

where the hat indicates a three dimensional, spatial Fourier transform of an underlying quantity, and $\boldsymbol{\omega}$ is the wavenumber vector. The RTE for the fluctuating component of the intensity ($I' = I - \bar{I}$) in the spatial domain reads

$$s_j\frac{\partial I'}{\partial x_j} = \overline{\kappa}I_b' + \kappa'\bar{I}_b + \kappa'I_b' - \overline{\kappa}I' - \kappa'\bar{I} - \kappa'I' + (\overline{\kappa'I_b'} - \overline{\kappa'I'}), \tag{29}$$

which after applying the Fourier transform gives

$$i(s_j\omega_j)\widehat{I'} = \overline{\kappa}\widehat{I'}_b + \widehat{\kappa'}\bar{I}_b - \overline{\kappa}\widehat{I'} - \widehat{\kappa'}\bar{I}. \tag{30}$$

Second order terms, $\kappa'I_b'$ and $\kappa'I'$, can be neglected in non-reactive turbulent flows, as demonstrated in Refs. [3,6,8,10]. The Fourier transform of the intensity fluctuation $\widehat{I'}$ can then be expressed explicitly as

$$\widehat{I'} = \frac{\overline{\kappa}\widehat{I'}_b + \widehat{\kappa'}\bar{I}_b - \widehat{\kappa'}\bar{I}}{\overline{\kappa} + i(s_j\omega_j)}. \tag{31}$$

By substituting this relation back into (28), the Fourier transformed incident radiation fluctuations can be written as

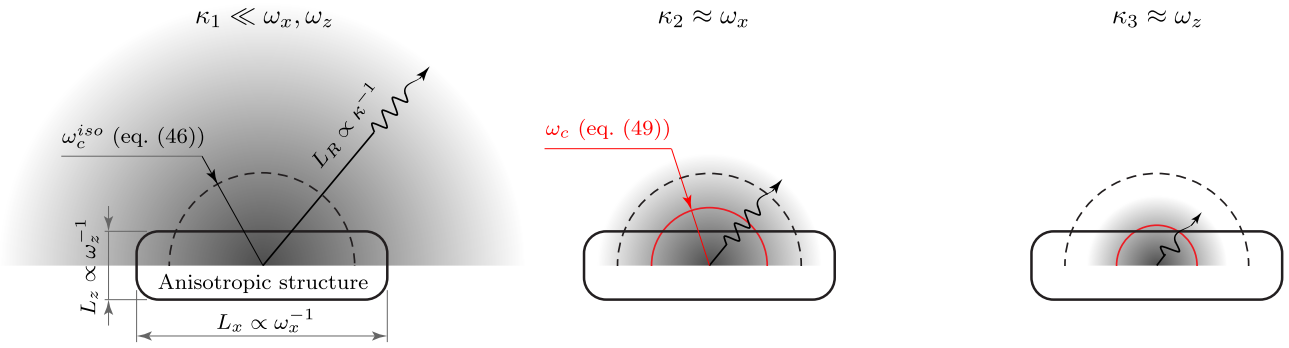

Fig. 2. Illustration of radiative effects on anisotropic structures in media with different κ values. L_x, L_z and L_R are the length scales in the streamwise direction, in the spanwise direction and for radiative transfer, respectively. The dashed circle represents the model isotropic structure described by ω_c^{iso} (independent of κ). The red circle shows the correction to properly reflect the anisotropic structure.

$$\widehat{G'} = \underbrace{\frac{\overline{\kappa}\widehat{I'}_b}{\pi}\int_{4\pi}\frac{1}{\overline{\kappa}+i(s_j\omega_j)}d\Omega}_{\mathcal{G}_1} + \underbrace{\frac{\widehat{\kappa'}\bar{I}_b}{\pi}\int_{4\pi}\frac{1}{\overline{\kappa}+i(s_j\omega_j)}d\Omega}_{\mathcal{G}_2} - \underbrace{\frac{\widehat{\kappa'}}{\pi}\int_{4\pi}\frac{\bar{I}}{\overline{\kappa}+i(s_j\omega_j)}d\Omega}_{\mathcal{G}_3}. \tag{32}$$

In order to solve the integrals, it is convenient to split them into a real and an imaginary part. The integrand in both $\mathcal{G}_1$ and $\mathcal{G}_2$ can then be written as

$$\frac{1}{\overline{\kappa}+i(s_j\omega_j)} = \frac{\overline{\kappa}}{\overline{\kappa}^2+(s_j\omega_j)^2} - i\frac{(s_j\omega_j)}{\overline{\kappa}^2+(s_j\omega_j)^2}. \tag{33}$$

Using a variable transformation $\mu = (s_j\omega_j)/\omega$, as introduced by Soufiani in [14], allows to integrate both terms to

$$\int_{4\pi}\frac{\overline{\kappa}}{\overline{\kappa}^2+(s_j\omega_j)^2}d\Omega = \frac{4\pi}{\omega}\operatorname{atan}\left(\frac{\omega}{\overline{\kappa}}\right), \tag{34}$$

$$\int_{4\pi}\frac{(s_j\omega_j)}{\overline{\kappa}^2+(s_j\omega_j)^2}d\Omega = 0, \tag{35}$$

where $\omega = \|\boldsymbol{\omega}\|$. Note, the integral of the imaginary part is zero, such that the final expressions for $\mathcal{G}_1$ and $\mathcal{G}_2$ are

$$\mathcal{G}_1 = 4\overline{\kappa}\frac{\widehat{I'}_b}{\omega}\operatorname{atan}\left(\frac{\omega}{\overline{\kappa}}\right), \tag{36}$$

$$\mathcal{G}_2 = 4\bar{I}_b\frac{\widehat{\kappa'}}{\omega}\operatorname{atan}\left(\frac{\omega}{\overline{\kappa}}\right). \tag{37}$$

The term $\mathcal{G}_3$ requires a different treatment due to the presence of the non-isotropic quantity $\bar{I}$. As a crude approximation, let us assume an isotropic $\bar{I}$ field, i.e. $\bar{I}$ being independent of Ω. The implications of this approximation will be discussed later. In this case, the integration gives an equivalent result as for $\mathcal{G}_1$ and $\mathcal{G}_2$ above, namely

$$\mathcal{G}_3 \approx 4\bar{I}\frac{\widehat{\kappa'}}{\omega}\operatorname{atan}\left(\frac{\omega}{\overline{\kappa}}\right). \tag{38}$$

Since $\bar{I}$ has been assumed is isotropic, the mean incident radiation reduces to $\overline{G} = 4\bar{I}$, such that

$$\mathcal{G}_3 \approx \overline{G}\frac{\widehat{\kappa'}}{\omega}\operatorname{atan}\left(\frac{\omega}{\overline{\kappa}}\right). \tag{39}$$

Finally, the sum of the three individual terms gives the approximation of the incident radiation fluctuations in a Fourier transformed domain

$$\widehat{G'} \approx \overline{\kappa}\frac{\widehat{E'}}{\omega}\operatorname{atan}\left(\frac{\omega}{\overline{\kappa}}\right) + \overline{E}\frac{\widehat{\kappa'}}{\omega}\operatorname{atan}\left(\frac{\omega}{\overline{\kappa}}\right) - \overline{G}\frac{\widehat{\kappa'}}{\omega}\operatorname{atan}\left(\frac{\omega}{\overline{\kappa}}\right), \tag{40}$$

where $4I_b$ has been replaced by E in the first and second term. Eq. (40) relates the Fourier transform of G' to $\widehat{E'}$ and $\widehat{\kappa'}$. In particular, these are scaled by a real function of the wavenumber $(1/\omega \cdot \operatorname{atan}(\omega/\overline{\kappa}))$. The lack of an imaginary part in the scaling function implies that $\widehat{G'}$ has no direct phase shift when compared to $\widehat{E'}$ and $\widehat{\kappa'}$. The rotational phase shift produced by the presence of an imaginary part can only be caused by the long-range action of $\bar{I}$ in $\mathcal{G}_3$, which propagates local absorption coefficient fluctuations from other directions. However, by employing the isotropic assumption, the mean intensity ($\bar{I}$), which couples the local κ' to G', is considered equal coming from all directions.

To obtain a closed expression for $\widehat{G'}$ as a function of θ', it is necessary to replace ω with one characteristic value, namely ω_c. After collecting terms with κ' and replacing ω with ω_c, Eq. (40) can be written as

$$\widehat{G'} \approx \underbrace{\frac{\overline{\kappa}}{\omega_c}\operatorname{atan}\left(\frac{\omega_c}{\overline{\kappa}}\right)}_{\text{not } f(\omega)}\cdot\widehat{E'} + \underbrace{\frac{\overline{E}-\overline{G}}{\omega_c}\operatorname{atan}\left(\frac{\omega_c}{\overline{\kappa}}\right)}_{\text{not } f(\omega)}\cdot\widehat{\kappa'}. \tag{41}$$

This entails that the shape of the G spectrum is entirely defined by the E and κ spectra. If this is done, an inverse Fourier transform of Eq. (41) yields

$$G' \approx \frac{\overline{\kappa}}{\omega_c}\operatorname{atan}\left(\frac{\omega_c}{\overline{\kappa}}\right)\cdot E' + \frac{\overline{E}-\overline{G}}{\omega_c}\operatorname{atan}\left(\frac{\omega_c}{\overline{\kappa}}\right)\cdot\kappa'. \tag{42}$$

Substituting $E' = f_E\theta'$ and $\kappa' = f_\kappa\theta'$ yields

$$G' \approx \left(\frac{\overline{\kappa}}{\omega_c}\operatorname{atan}\left(\frac{\omega_c}{\overline{\kappa}}\right)\cdot f_E + \frac{\overline{E}-\overline{G}}{\omega_c}\operatorname{atan}\left(\frac{\omega_c}{\overline{\kappa}}\right)\cdot f_\kappa\right)\cdot\theta', \tag{43}$$

and finally, the expression for the third and last coefficient of proportionality f_G can be stated as follows

$$f_G = \left(\frac{f_E\overline{\kappa} + f_\kappa(\overline{E}-\overline{G})}{\omega_c}\right)\operatorname{atan}\left(\frac{\omega_c}{\overline{\kappa}}\right). \tag{44}$$

4.4. Determining ω_c for anisotropic turbulence

To obtain a formal expression for Eq. (42), the parameter ω_c, which represent the length scale of the average energy-containing temperature structure, requires a closure. In homogeneous isotropic turbulence it can be defined as the expected value of $\boldsymbol{\omega}$ based on the normalized turbulent temperature power density spectrum.

$$\omega_c = \left\|\int_0^\infty \frac{\boldsymbol{\omega}\mathcal{S}_\theta(\boldsymbol{\omega})}{\overline{\theta'^2}}d\boldsymbol{\omega}\right\|, \tag{45}$$

where $\mathcal{S}_\theta$ is the spectrum of temperature fluctuations. Note, temperature has been chosen since κ and E are fully defined by θ. The integrand in Eq. (45) represents the normalized distribution

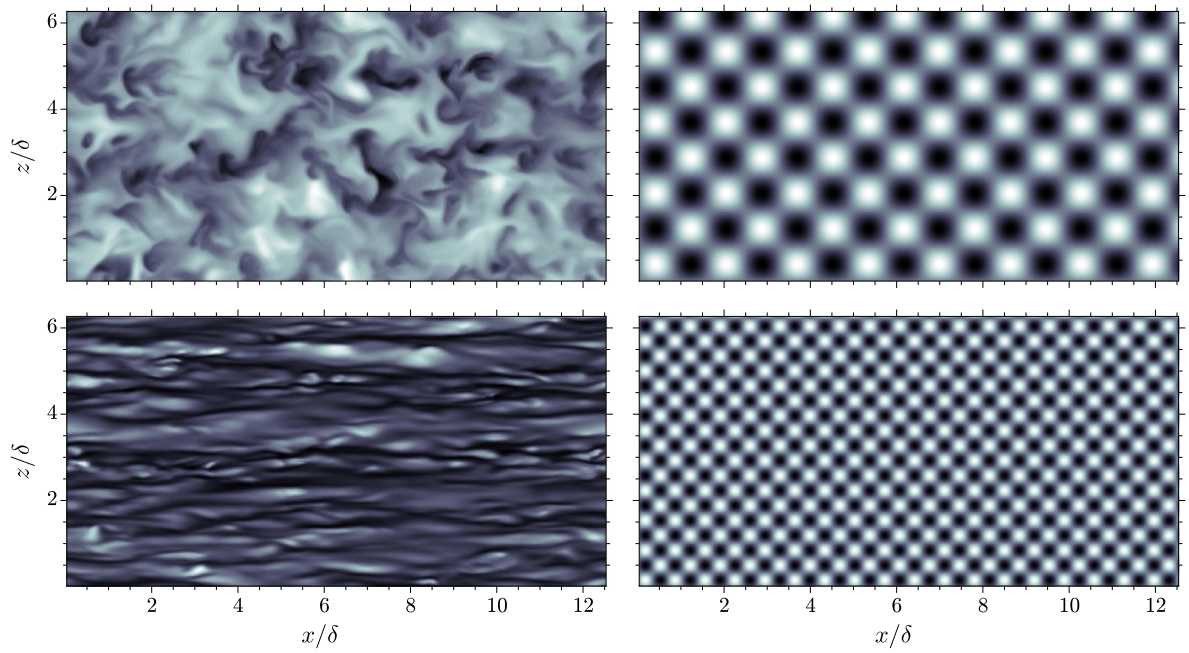

Fig. 3. Visualization of the "collapsing" procedure that retrieves a characteristic ω_c to describe the radiative field. On the left: temperature fields at $y/\delta = 1.1$ (top) and $y/\delta = 1.97$ (bottom). On the right: corresponding single mode fields denoted by ω_c.

of temperature fluctuations over all scales, and as such, it is an appropriate choice to define the length scale of the energy containing eddies.

In a channel flow, however, temperature structures are anisotropic due to the presence of walls. In mathematical terms, this means that the inhomogeneous wall-normal direction does not allow the application of the Fourier transform in Eq. (29) in all spatial directions. As such, $\partial_y \widehat{I'}$ would remain in Eq. (30), preventing the derivation of an analytic solution. To overcome this, we will only account for the anisotropic temperature structures in the turbulent flow and assume that the fluctuations of the incident radiation emerge from an unbounded domain without the presence of walls.

If we follow the same approach as in homogeneous isotropic turbulence, the dimension of the scales can be inferred from the one-dimensional temperature spectrum in span-wise and stream-wise directions. The resulting ω_c^{iso} is then obtained as

$$\omega_c^{iso} = \left[\left(\frac{\int_0^\infty \omega_x \mathcal{S}_\theta(\omega_x) d\omega_x}{\overline{\theta'^2}} \right)^2 + \left(\frac{\int_0^\infty \omega_z \mathcal{S}_\theta(\omega_z) d\omega_z}{\overline{\theta'^2}} \right)^2 \right]^{0.5}. \quad (46)$$

As described in Ref. [12], anisotropic temperature structures are associated with an absorption penalty due to a "non-spherical surface to volume ratio" when compared to the isotropic nature of radiative emission. Fig. 2 shows an example of an anisotropic structure immersed in flows of different absorption coefficients (increasing from left to right). L_R represents the mean-path length of radiative heat transfer which is inversely proportional to κ. If κ is much smaller than the structure's wavenumbers (Fig. 2, left), radiation escapes almost equally from all directions. It is clear that an isotropic structure with wavenumber ω_c^{iso} results in an equivalent behaviour, since the shape of the structure does not influence the absorption process. On the other hand, if κ^{-1} is comparable to the length scales of the temperature structure (center), radiation is allowed to escape in one direction while being absorbed in another. However, the isotropic structure described by ω_c^{iso} (dashed circle in Fig. 2), results in complete absorption in all directions. In this case, a more suitable approximation would be a smaller isotropic structure which allows for escaping radiation, as shown by the red circles in Fig. 2. Therefore, it is necessary to increase ω_c^{iso} to account for this effect. It is crucial to notice that the correction of ω_c^{iso} must be larger as κ grows, as demonstrated in Fig. 2 by comparing the central and right image. As a first approximation, it is possible to correct for the structure's anisotropy by including the radiative length scale L_R in the definition of ω_c. By doing so, the increase of the absorption penalty with increasing κ is naturally

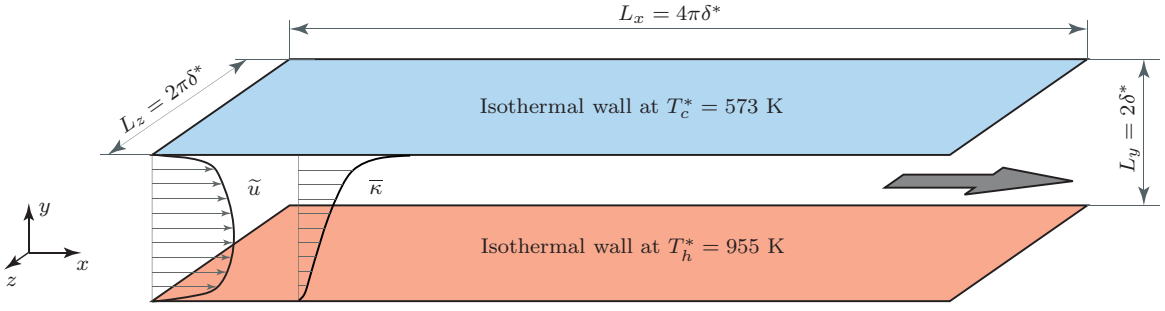

Fig. 4. Schematic displaying the computational domain. The profiles shown are the Favre averaged streamwise velocity ($\widetilde{u}$) and Reynolds averaged Planck-mean absorption coefficient ($\overline{\kappa}$) for case H.

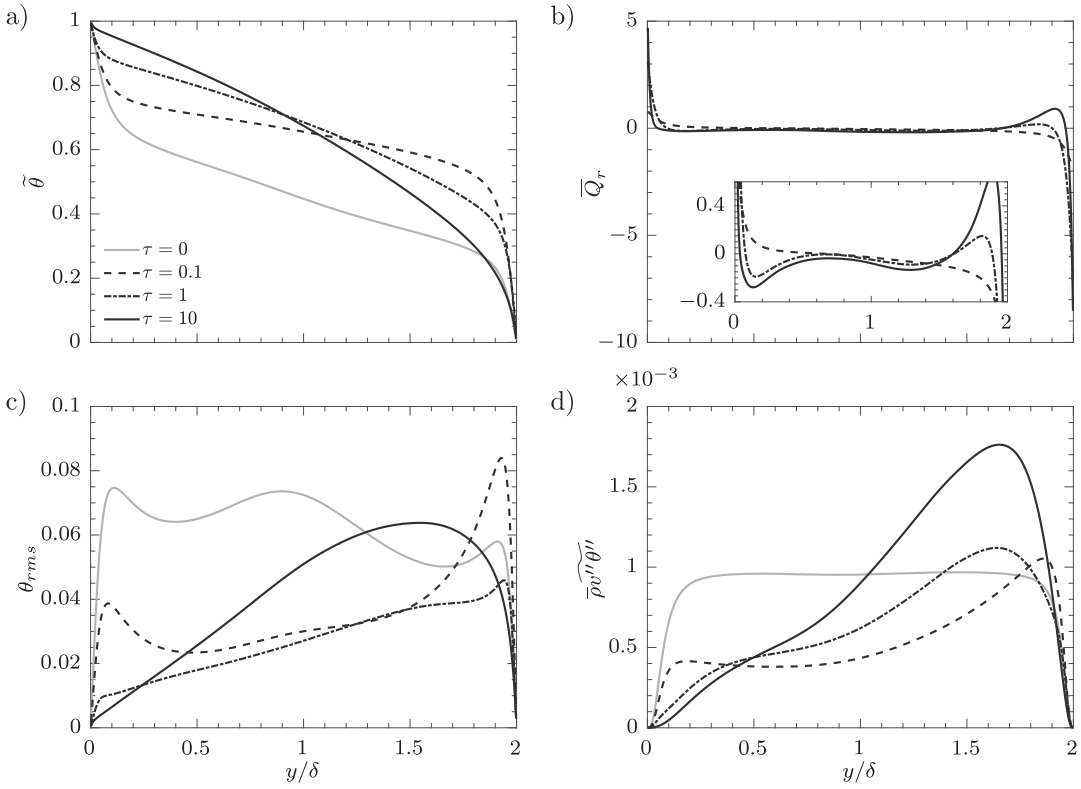

Fig. 5. Mean quantities for gray gas cases. Top left: Favre averaged temperature profile. Top right: Reynolds averaged radiative power. Bottom left: temperature rms profiles. Bottom right: turbulent heat flux. Solid gray line: no radiation, dashed line: G01 case, dashed-dotted line: G1 case, solid black line: G10 case.

included. Incorporating L_R in ω_c results in

$$\omega_c \propto \sqrt{{L_x}^{-2} + {L_z}^{-2} + {L_R}^{-2}}. \tag{47}$$

However, it yet has to be decided how much absorption to account for when defining the radiative length scale. From Beer's law, L_R can be expressed as

$$L_R = \frac{\ln(X)}{\kappa}, \tag{48}$$

where X is the remaining radiative intensity after a certain distance L_R (in percentage). Mathematically speaking, complete absorption occurs at $L_R \to \infty$, which would result in $\omega_c = \omega_c^{iso}$. If 90% of absorbed radiation is accounted for, the corrected characteristic wavenumber can be expressed as

$$\omega_c = \left[\left(\frac{\int_0^\infty \omega_x \mathcal{S}_\theta(\omega_x) d\omega_x}{\overline{\theta'^2}} \right)^2 + \left(\frac{\int_0^\infty \omega_z \mathcal{S}_\theta(\omega_z) d\omega_z}{\overline{\theta'^2}} \right)^2 + \left(\frac{\overline{\kappa}}{\ln(10)} \right)^2 \right]^{0.5}. \tag{49}$$

An example of approximating all wavenumbers by one characteristic isotropic mode is visualized for the flow in a turbulent channel in Fig. 3. The contours on the left show the temperature field at two wall parallel planes, namely at a plane close to a channel center (top) and a plane close to a wall (bottom). κ_p is roughly 8 and 12 for the top and bottom contour, respectively. The contours on the right show the corresponding isotropic fields "seen" by G'. These are characterized by a single mode described by ω_c as calculated by Eq. (49) (the amplitude of the field is completely irrelevant since ω_c provides only a scaling parameter). Consistent with the theory developed in Ref. [12] and the above reasoning, the dominant mode of anisotropic structures at $y/\delta = 1.97$ correspond to the largest wavenumber of the field.

5. Numerical implementation and studied cases

The computational domain for the channel flow is outlined as follows: streamwise length $L_x = 4\pi\delta^*$, spanwise length $L_z = 2\pi\delta^*$ and wall normal height $L_y = 2\delta^*$, where δ^* is the half channel height. The number of grid points used is $192 \times 192 \times 192$. The corresponding grid spacing in terms of plus units is $\Delta x^+ \approx 12.5$, $\Delta y_w^+ \approx 0.38$ and $\Delta z^+ \approx 6.3$. The channel is periodic in the streamwise and spanwise direction both in terms of flow and radiative heat transfer. The Navier–Stokes equations have been solved using a pseudo-spectral method in the periodic directions, and a sixth order staggered compact finite difference scheme for the discretization of derivatives in the wall normal direction. A pressure correction scheme is employed based on the projection method, while a pressure gradient is applied in the streamwise direction in order to maintain a constant Reynolds number based on bulk velocity. For details and validation of the DNS code, the reader is referred to Refs. [15–17].

The simulations consist of three gray gas cases (G01, G1 and G10) and three non-gray gas cases (H, C and P). The synthetic spectra for the three non-gray cases have been produced to provide a different level of spectral variability of κ_λ such that, as it will be explained in more details in Section 7, the influence of different absorption spectra can be assessed. All cases share the same flow parameters (Reynolds, Prandtl, Planck number) defined in Eq. (7), as well as the same boundary conditions, spatial mesh and Navier–Stokes solver. The flow is bounded by two black isothermal walls ($\varepsilon_w = 1$) kept at 573 K (top) and 955 K (bottom), respectively. The difference between the cases lies in the description of radiative heat transfer. The details of the latter on a case to case basis are shown in Table 1.

In the gray gas cases, a finite volume method (FVM) [18] with a high-order resolution CLAM spatial discretization scheme, as de-

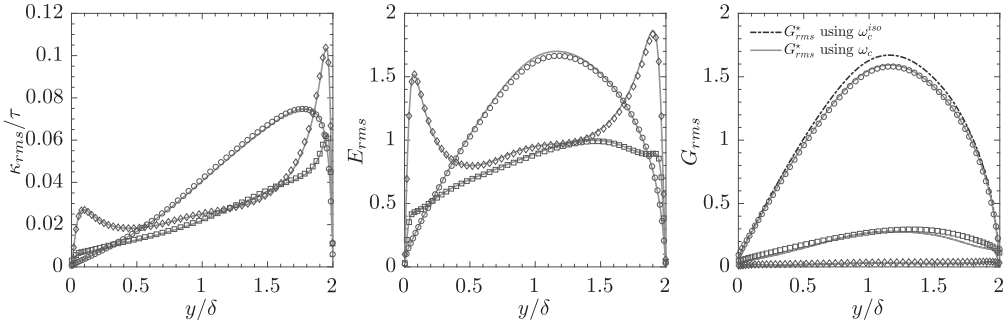

Fig. 6. Comparison between radiative field fluctuations from DNS (symbols) and estimated by using θ_{rms} and $\overline{\theta}$ (gray lines). Diamonds: $\tau = 0.1$. Squares: $\tau = 1$. Circles: $\tau = 10$.

Table 1
Details of simulated cases.

Case	κ^*	τ	Method	discretization
base	0	0	–	–
G01	$\kappa^*(\theta)$	0.1	FVM	96 angles
G1	$\kappa^*(\theta)$	1	FVM	96 angles
G10	$\kappa^*(\theta)$	10	FVM	384 angles
H	$\kappa^*_\lambda(H_2O)$	8.02	MCM	$15 \cdot 10^3$ rays per cell
C	$0.1\kappa^*_\lambda(CO_2)$	2.99	MCM	$9 \cdot 10^3$ rays per cell
P	$0.1\kappa^*_\lambda(H_2O)$+2	2.79	MCM	$9 \cdot 10^3$ rays per cell

scribed by Coelho [19] has been used. Cases G01 and G1 employ a total of 96 independent directions, while for case G10, due to the higher absorption level, 384 directions have been used. For the non-gray gas cases, the radiative transfer equation has been solved with an optimized emission based reciprocal Monte Carlo formulation as described in Zhang et al. [20]. The Monte Carlo solver calculates the radiative source term on the full DNS mesh and is coupled to the fluid solver every 5 fluid time steps. The spectral description has been treated with a narrow band correlated-K formulation based on line-by-line spectra obtained from the HITRAN 2012 spectroscopy database [21]. The full spectra in the 500–1010 K temperature range (with a step of 10 K) have been divided into 119 and 130 narrow bands for H_2O and CO_2, respectively. 16 quadrature points for each narrow band have employed. 15000 rays per cell have been used for the optically thicker case (H), while for cases P and C 9000 rays per cell were sufficient, as the associated intrinsic variance results being lower than 1%. The Monte Carlo solver is executed on GPU, implemented via the programming language CUDA. Several techniques are employed in order to increase the level of parallelization and improve the efficiency of memory access and thread execution. For a detailed description of the implementation and validation of the Monte Carlo code, the reader is referred to Ref. [22].

6. Gray gas cases

This section is intended to verify the validity of the relations derived in Section 4 and to compare the predictions with the DNS data. Furthermore, the influence of a variable absorption coefficient on the turbulent temperature field is investigated. In a participating turbulent flow, velocity profiles and statistics are not directly connected to radiative heat transfer but are indirectly affected by the modification of the density profiles. Most of the published work regarding the modification of velocity due to radiation deal either with buoyant [7] or with supersonic cases [10]. On the other hand, in the simulated cases, gravity has been neglected and a low Mach number approximation has been employed. In addition, the density variations are relatively small (40% between the hot and the cold wall). Consequently, the effects of radiation on velocity are completely negligible. Since the velocity profiles are the same as for a well-known ideal gas turbulent channel flow, we will omit the analysis of the latter.

6.1. DNS results and validation of linear relations

Fig. 5 shows the profiles of Favre averaged non-dimensional temperature $\widetilde{\theta}$ and Reynolds averaged radiative heat source $\overline{Q}_r$ (the inlay shows a zoom on the y-axis), as well as temperature root-mean-square values θ_{rms}, and turbulent heat flux $\overline{\rho}\widetilde{v''\theta''}$. Radiative heat transfer causes a growth in bulk temperature and, upon increasing optical thickness, the temperature gradient rises in the core of the channel while reducing near the walls. The mean radiative source can be expressed as

$$\overline{Q}_r = \overline{\kappa}(\overline{E} - \overline{G}) + (\overline{\kappa' E'} - \overline{\kappa' G'}). \tag{50}$$

The second order terms will be analyzed and modeled in Section 9. Nevertheless, it has been already demonstrated that $\overline{\kappa' E'}$ and $\overline{\kappa' G'}$ are negligible in non-reactive flows [3,6,8,10]. Therefore, it is possible to account for mean radiative heat transfer effects as only influenced by $\overline{\kappa}$. Profiles of θ_{rms} are presented in Fig. 5(c). Again, the

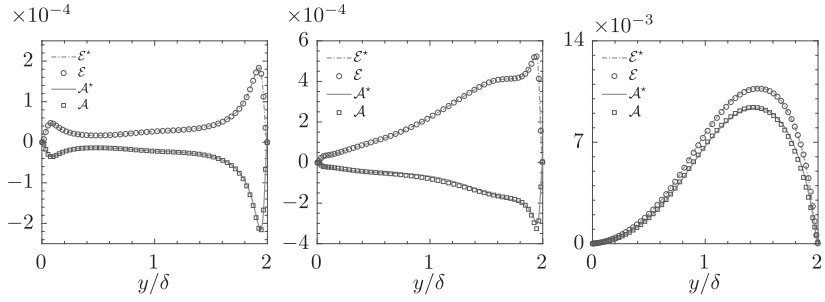

Fig. 7. Comparison between absorption and emission term from DNS (symbols) and estimated by using $\overline{\theta'^2}$ and $\overline{\theta}$ (lines). Left: $\tau = 0.1$, center: $\tau = 1$, right: $\tau = 10$.

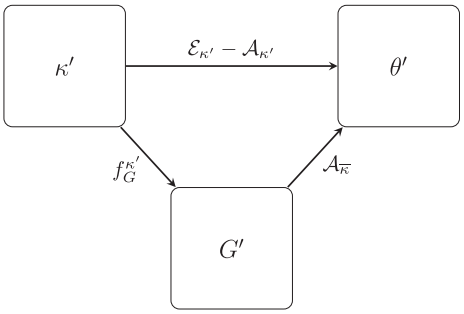

Fig. 8. Effect of κ' on θ'.

typical behaviour of temperature fluctuation in the presence of a fluctuating radiative field is observed. Namely, temperature fluctuations are reduced due to the action of a turbulent emission field that acts as a damping mechanism. This occurs throughout the channel but has a larger impact near the walls where temperature structures are thin and streaky. At a higher τ, θ_{rms} are recovered by the presence of a stronger fluctuating G field. The recovery occurs in the core of the channel where quasi-isotropic structures are more efficient in retaining the emitted energy. The peak of the recovery is slightly shifted to the top of the channel where $\overline{\kappa}$ is larger. The trend of θ_{rms} induces the same behaviour in the turbulent heat flux shown in Fig. 5(d).

To validate the relations derived in Section 4, Fig. 6 shows the comparison of radiative field fluctuations (κ_{rms}, E_{rms} and G_{rms}) directly obtained from DNS with the values estimated from the linear relations. In particular, since the coefficients only depend on averaged quantities, the estimations take the following form

$$\kappa^{\star}_{rms} = f_{\kappa}\theta_{rms} \quad E^{\star}_{rms} = f_E\theta_{rms} \quad G^{\star}_{rms} = f_G\theta_{rms}, \tag{51}$$

where the star superscript (here and in the following sections) indicates that the value has been estimated. The right-hand side of relations in (51) is calculated from DNS data. Fig. 6 proves that the radiative field fluctuations are well represented by their approximation. G_{rms} is estimated using both ω_c^{iso} (dashed-dotted line), and ω_c (grey solid line). Except for case G10, the two profiles collapse onto each other. Indeed, it is necessary to correct for anisotropic structures only if $L_R \approx \omega_z$, meaning if the optical thickness is large enough (see Fig. 2).

6.2. Impact of absorption coefficient fluctuations on temperature variance

The effect of radiative heat transfer on the turbulent temperature field manifests through the radiation term $\mathcal{R}$ in the Favre averaged temperature variance equation, which, neglecting terms containing $\overline{\theta''}$, reads

$$\overline{\rho}\frac{D\widetilde{\theta''^2}}{Dt} = -2\overline{\rho}\widetilde{u_j''\theta''}\frac{\partial\widetilde{\theta}}{\partial x_j} - \frac{\partial\overline{\rho}\widetilde{u_j''\theta''^2}}{\partial x_j} + \frac{2}{RePr}\left(\frac{1}{2}\frac{\partial^2\overline{\theta'^2}}{\partial x_j^2} - \overline{\left(\frac{\partial\theta'}{\partial x_j}\right)^2} - \frac{1}{Pl}\underbrace{\overline{Q_r'\theta'}}_{\mathcal{R}}\right). \tag{52}$$

The magnitude of the radiation term depends on the optical thickness of the medium. As τ tends to zero the radiative terms disappears. The same occurs when $\tau \to \infty$. Around $\tau = 10$, the radiative term is dominant and balances turbulent production. A detailed analysis of the temperature variance budgets in a radiative flow can be found in Ref. [8] and in our recent work [12]. The radiation term $\mathcal{R}$ can be decomposed in an emission term $\mathcal{E}$ and an absorption term $\mathcal{A}$ as

$$\mathcal{R} = \underbrace{\overline{(\kappa E)'\theta'}}_{\mathcal{E}} - \underbrace{\overline{(\kappa G)'\theta'}}_{\mathcal{A}}. \tag{53}$$

$\mathcal{E}$ and $\mathcal{A}$ can be expanded, neglecting third order correlations, into terms depending on $\overline{\kappa}$ and on κ' to highlight the different influence of the mean and the fluctuating part of the absorption

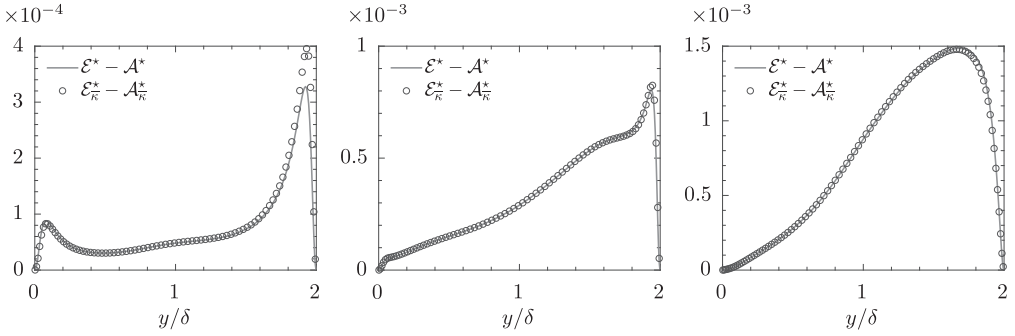

Fig. 9. Comparison between radiation term estimated using the full absorption coefficient (symbols) and using only the terms depending on the mean absorption coefficient (lines). Left: $\tau = 0.1$, center: $\tau = 1$, right: $\tau = 10$.

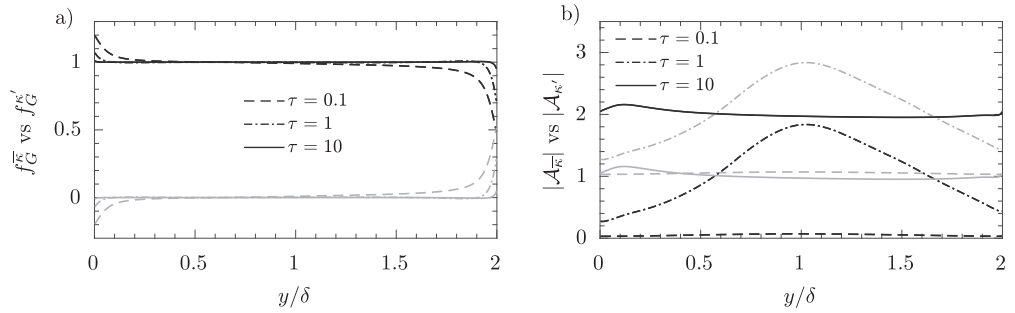

Fig. 10. Influence of κ' on G'. (*a*): comparison between $f_G^{\overline{\kappa}}$ (black) and $f_G^{\kappa'}$ (gray) normalized by f_G. (*b*): comparison between $\mathcal{A}_{\overline{\kappa}}$ (black) and $\mathcal{A}_{\kappa'}$ (gray) normalized by $\mathcal{A}$.

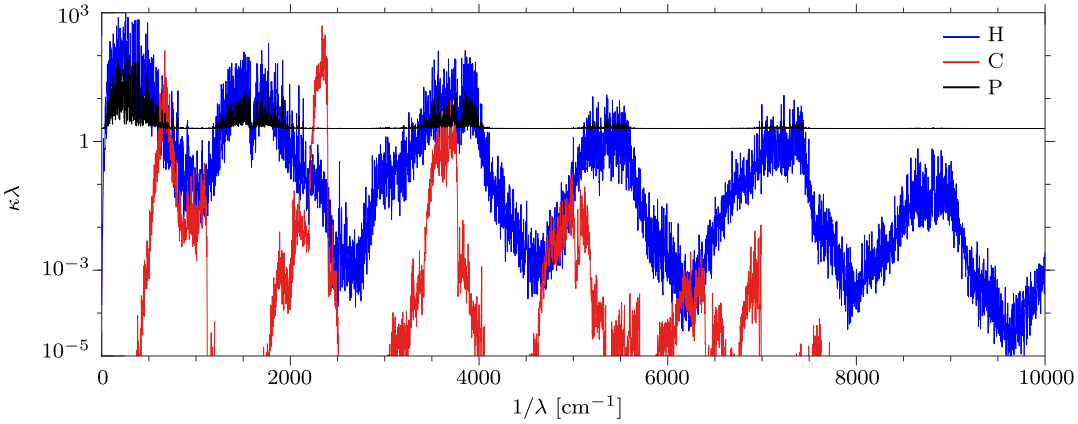

Fig. 11. Absorption spectrum at 770 [K] and 1 [bar] for case H (blue), case C (red) and case P (black).

coefficient.

$$\mathcal{E} = \underbrace{\overline{E}\cdot\overline{\kappa'\theta'}}_{\mathcal{E}_{\kappa'}} + \underbrace{\overline{\kappa}\overline{E'\theta'}}_{\mathcal{E}_{\overline{\kappa}}} \quad \mathcal{A} = \underbrace{\overline{G}\cdot\overline{\kappa'\theta'}}_{\mathcal{A}_{\kappa'}} + \underbrace{\overline{\kappa}\overline{G'\theta'}}_{\mathcal{A}_{\overline{\kappa}}}. \tag{54}$$

Substituting relations (17) in Eq. (54) yields estimations for $\mathcal{E}$ and $\mathcal{A}$

$$\mathcal{E} \approx \mathcal{E}^\star = \underbrace{\overline{E}f_\kappa\overline{\theta'^2}}_{\mathcal{E}^\star_{\kappa'}} + \underbrace{\overline{\kappa}f_E\overline{\theta'^2}}_{\mathcal{E}^\star_{\overline{\kappa}}} \quad \mathcal{A} \approx \mathcal{A}^\star = \underbrace{\overline{G}f_\kappa\overline{\theta'^2}}_{\mathcal{A}^\star_{\kappa'}} + \underbrace{\overline{\kappa}f_G\overline{\theta'^2}}_{\mathcal{A}^\star_{\overline{\kappa}}}. \tag{55}$$

Fig. 7 shows the comparison between the estimated terms and the values obtained by DNS, demonstrating that the derived linear relations are capable of accurately predicting the radiation terms.

To isolate the effects of κ' it is possible to further decompose f_G into a $\overline{\kappa}$ and a κ' dependent term as

$$f_G^{\overline{\kappa}} = \frac{f_E\overline{\kappa}}{\omega_c}\mathrm{atan}\left(\frac{\omega_c}{\overline{\kappa}}\right) \quad f_G^{\kappa'} = \frac{f_\kappa(\overline{E}-\overline{G})}{\omega_c}\mathrm{atan}\left(\frac{\omega_c}{\overline{\kappa}}\right), \tag{56}$$

with $f_G = f_G^{\overline{\kappa}} + f_G^{\kappa'}$. Fig. 8 shows the coupling between κ' and θ'. κ' can influence θ' directly, through $\mathcal{E}_{\kappa'} - \mathcal{A}_{\kappa'}$, or indirectly through the modification of G'.

The direct impact of κ' on θ' can be visualized by comparing $\mathcal{E}_{\overline{\kappa}} - \mathcal{A}_{\overline{\kappa}}$ to $\mathcal{E}_{\kappa'} - \mathcal{A}_{\kappa'}$. This comparison is displayed in Fig. 9 for cases G01 (left), G1 (center) and G10 (right). The symbols show the full radiation term $\mathcal{R}$, while the lines are the radiation term calculated taking into account $\overline{\kappa}$ contributions only. Accounting for a mean absorption coefficient is enough to retrieve the full radiation term, thereby demonstrating that κ' has a negligible direct influence on temperature fluctuations.

Furthermore, the comparison between $f_G^{\overline{\kappa}}$ and $f_G^{\kappa'}$ is shown in Fig. 10(a). The two terms are normalized by the total f_G to highlight their relative magnitude. The results prove that $f_G^{\overline{\kappa}}$ is always dominant over the κ' term. Moreover, the relative difference between the two terms increases with a larger optical thickness. A small influence of $f_G^{\kappa'}$ can be detected in the lower optical thickness case (G01). To quantify the indirect effect of κ', it is necessary to verify the impact of the absorptive term $\mathcal{A}_{\overline{\kappa}}$, which connects G' to θ' (see Fig. 8). Fig. 10(b) shows the comparison between the absorptive term depending on κ' (in gray) and $\mathcal{A}_{\overline{\kappa}}$ (in black). For a low optical thickness, the latter tends to zero, which indirectly proves that $G' = 0$ in the limit of $\tau \to 0$. As a consequence, despite $f_G^{\kappa'}$ having a non-negligible value in the low optical thickness case, the low magnitude of $\mathcal{A}_{\overline{\kappa}}$ nullifies any possible influence of κ'.

In conclusion, it has been demonstrated that in high-temperature non-reacting flows, TRI can be accounted for by the variation of the mean absorption coefficient alone. The presence of κ' can be neglected completely, independently from the value of the optical thickness.

7. Non-gray gas cases

This section is intended to investigate how a wavelength dependent absorption coefficient modifies TRI. The absorption spectra of cases H, C and P, as defined in Table 1, are specifically designed to compare TRI in flows with different spectral variability. The non-dimensional absorption spectra for the three cases at 770 K and 1 bar are shown in Fig. 11. The spectrally averaged parameters for the three cases are shown in Table 2.

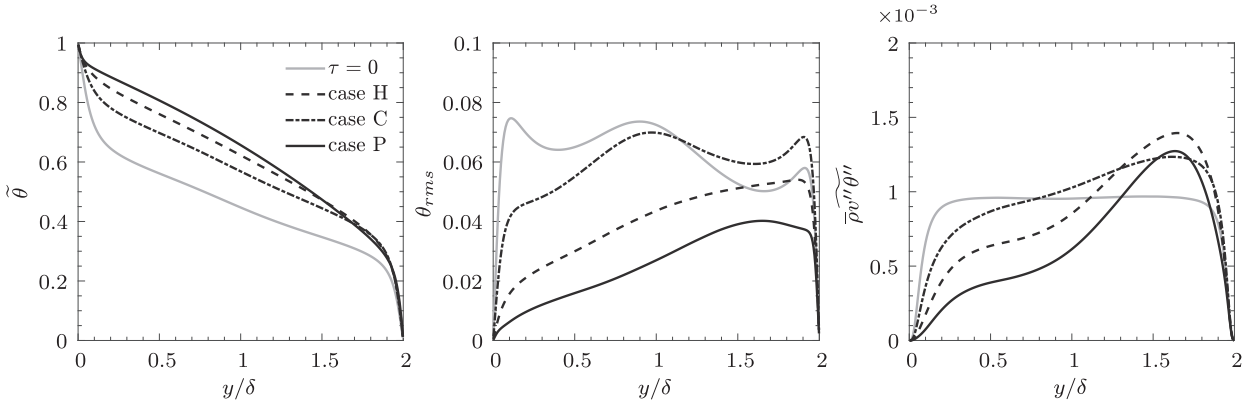

Fig. 12. Mean quantities for non-gray gas cases. Left: Favre averaged temperature profile. Center: temperature RMS profiles. Right: turbulent heat flux. Solid gray line: no radiation, dashed line: case H, dashed-dotted line: case C, solid black line: case P.

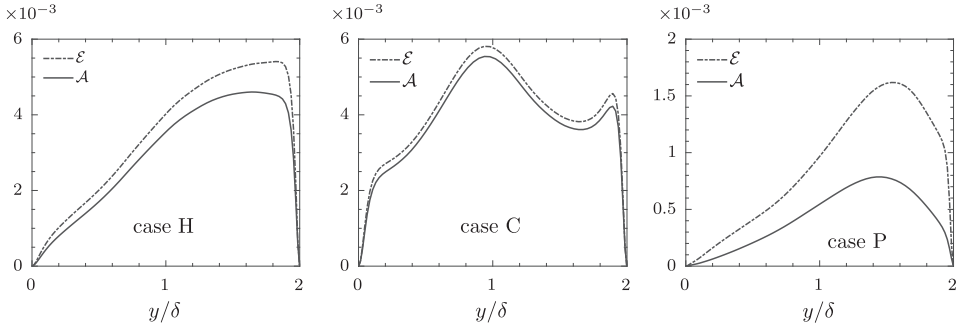

Fig. 13. Radiation terms $\mathcal{E}$ and $\mathcal{A}$. Left: case H. Center: case C. Right: case P.

Table 2
Optical thickness and global transmissivity for the non-gray cases.

Case	H	C	P
τ	8.02	2.99	2.79
t	0.51	0.88	0.10

The categorization of TRI with non-gray gases is difficult. Based on the optical thickness of the channel, one has $\tau_H > \tau_C \gtrsim \tau_P$, suggesting that TRI in H is characterized by an optically thicker behaviour when compared to C and P. Contrarily, the transmissivity (Eq. (15)) for these cases satisfies $t_P < t_H < t_C$, implying that case C is the most transparent. How the TRI mechanism manifests itself, is, therefore, not clearly described by these two parameters.

Fig. 12 shows several quantities of interest for the three investigated cases. The figures present plots of Favre-averaged temperature, temperature rms and turbulent heat flux profiles on the left, center and right, respectively. Contrarily to what could be expected, all profiles of H are enclosed in between those of C and P. Moreover, case P and C show very different profiles, despite having similar average absorption coefficients. Global transmissivity seems to order correctly the mean temperature profiles but fails to completely capture the physics occurring. For example, the bulk temperature is lower for case C than for case P, signifying a lower bulk Q_r in case C. By taking into account Eq. (50), this could be the effect of two contrasting causes: (1) a lower $\overline{\kappa}$ (more transparent case), (2) a lower $\overline{E} - \overline{G}$, which is typical of a higher optical thickness fluid. Since C and P have very similar $\overline{\kappa}_p$, it is clear that the correct option is the second.

This is corroborated by the fact that also TRI in case C is akin to an optical thick case, as can be noticed by the larger temperature gradient near the walls. This indicates that the highly anisotropic temperature structures close to the boundaries are sensitive to G', enabling a higher turbulent heat transfer from the near wall region to the core of the channel. Evidence can be found by inspecting the θ_{rms} profiles in Fig. 12(b), which indeed is as high as for a non-radiative case. As a consequence, a larger turbulent heat transfer is observed when compared to the other radiative cases, especially near the hot wall (Fig. 12(c)). The results for case C appear more similar to a gray gas case with $\tau > 10$ than what can be predicted using τ or t.

On the other hand, case P shows optically thinner TRI when compared to the other non-gray cases. This is substantiated by the lower θ_{rms} which are proof of lower G fluctuations. A confirmation of the above reasoning is found by inspecting the radiation terms $\mathcal{E}$ and $\mathcal{A}$, shown in Fig. 13. The left plot corresponds to profiles of case H, while center and right plots show values for case C and P, respectively. The magnitude of $\mathcal{E}$ and $\mathcal{A}$ are highest for case C, followed by H and P. In particular, it is possible to notice that for case C, $\mathcal{A} \approx \mathcal{E}$, proving that the incident fluctuation field is tightly correlated to the temperature field. This is typical of an optically thick flow, as it will be explained in the next section. Following the analysis of the DNS results, the categorization of TRI in the non-gray cases suggest that the three cases effectively behave as decreasing in optical thickness when going from C to H and then to P.

8. How to categorize TRI in non-gray gases?

8.1. "Effective" TRI optical thickness

Due to the high variability of the absorption spectra of a non-gray gas, using τ or t to categorize TRI is ambiguous and may even lead to wrong conclusions, as clearly demonstrated in Section 7. For this reason, it is necessary to identify a new parameter to clearly characterize TRI for a wide range of optical thicknesses, which is not trivial due to the non-monotonic behaviour of most variables and their complex non-linear interactions. Starting from the gray gas cases, it is possible to observe a consistent trend, which will help to identify the unique mechanisms of TRI. Taking into account the two extremes of an optically thin and thick gas, it can be stated that

$$E' \gg G' \to 0, \quad \text{if} \quad \tau \to 0 \tag{57}$$

$$E' - G' \ll G' \to E', \quad \text{if} \quad \tau \to \infty. \tag{58}$$

In the optically thin limit, only emission produces fluctuations, while in the optically thick limit, emission and absorption fluctuations balance. We claim that, for a gray gas, increasing or decreasing τ can be linked to approaching either limiting behaviour, without the necessity of analyzing any other quantity to characterize TRI. As a consequence, if two flows have substantially dif-

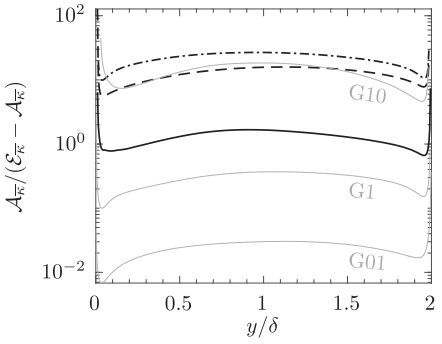

Fig. 14. Profiles of $\mathcal{A}_{\overline{\kappa}}/(\mathcal{E}_{\overline{\kappa}} - \mathcal{A}_{\overline{\kappa}})$ for the different gray and non-gray gas cases. dashed line: case H, dashed-dotted line: case C, solid line: case P. The thin gray lines show the gray gas cases.

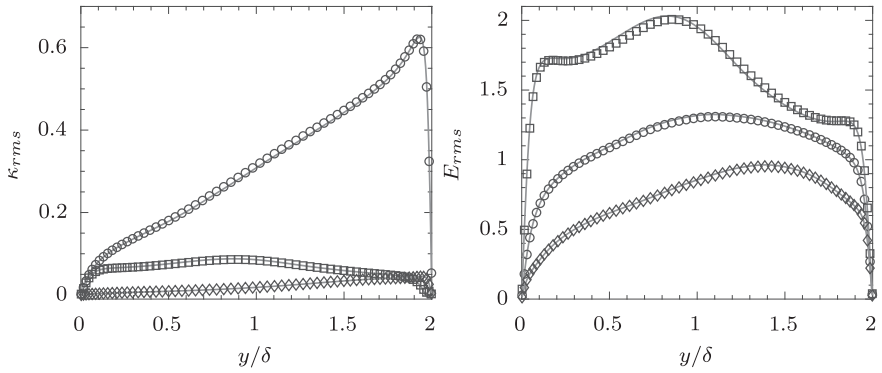

Fig. 15. Comparison of $\kappa^{\star}_{rms}$ and $E^{\star}_{rms}$ (gray lines) with κ_{rms} and E_{rms} obtained by DNS (symbols). Circles: case H, squares: case C, diamonds: case P.

ferent τ values, for example $\tau_1 > \tau_2$, it follows that $(E'_1 - G'_1)/G'_1 < (E'_2 - G'_2)/G'_2$. This means that incident radiation fluctuations approach emission fluctuations since radiation is absorbed closer to the emission point. More generally, using the decomposition of the radiation term $\mathcal{R}$, Eq. (54), this can be approximated by the following inequality

$$\left.\frac{\mathcal{A}_{\overline{\kappa}}}{\mathcal{E}_{\overline{\kappa}} - \mathcal{A}_{\overline{\kappa}}}\right|_{\tau_1} \gtrsim \left.\frac{\mathcal{A}_{\overline{\kappa}}}{\mathcal{E}_{\overline{\kappa}} - \mathcal{A}_{\overline{\kappa}}}\right|_{\tau_2 < \tau_1}. \tag{59}$$

Indeed, Fig. 14 confirms that for gray gas turbulence, the quantity in the above equation is monotonically associated to τ (see the gray lines). The definition of large and small optical thickness TRI can be related to the expressions in (57) and (58). Consequently, comparing optical depths, with regards to TRI, is interchangeable with comparing the quantities in expression (59).

On the other hand, for a non-gray gas this is not the case. Fig. 14 indeed confirms that the non-gray gas cases behave as if $\tau_C > \tau_H > \tau_P$. Neither the Planck-mean optical thickness τ nor the global transmissivity t can reflect this behaviour. Hence, it is necessary to derive a new spectrally integrated parameter to categorize TRI, which can allow a leading order comparison between non-gray and gray gas cases.

8.2. Derivation of a TRI based spectral averaging

The new parameter must be connected to TRI, so it is useful to employ the three correlations derived in Section 4 and adapt them when necessary for non-gray gases. f_κ and f_E do not require any modifications to account for spectrally varying absorption coefficients, since κ_p and E are spectrally integrated quantities. This is exemplified by Fig. 15, where it can be seen that the estimated profiles for κ_{rms} (left) and E_{rms} (right) match well with the data obtained from DNS. On the other hand, f_G must be modified to account for non-gray gases, due to the dependency on κ_λ, Eq. (11). If we assume that κ' (both κ'_λ and κ'_p) have a negligible influence on G, we can write

$$G' \approx \frac{1}{\overline{\kappa}_p}\int_0^\infty \overline{\kappa}_\lambda G'_\lambda d\lambda, \text{ where } G'_\lambda = \frac{1}{\pi}\int_{4\pi} I'_\lambda d\Omega. \tag{60}$$

Since a single wavelength can be described by a gray gas, G'_λ is properly predicted by

$$G'_\lambda \approx 4\overline{\kappa}_\lambda \frac{I'_{b,\lambda}}{\omega_c}\operatorname{atan}\left(\frac{\omega_c}{\overline{\kappa}_\lambda}\right). \tag{61}$$

Additionally, since G' is a spectrally integrated quantity, it can be approximated with a gray gas having a fictitious absorption coefficient κ_g. As a consequence, the combination of Eqs. (60) and (61) yields a constitutive relation for κ_g,

$$4I'_b \frac{\kappa_g}{\omega_c}\operatorname{atan}\frac{\omega_c}{\kappa_g} \approx \frac{1}{\overline{\kappa}_p}\int_0^\infty \overline{\kappa}^2_\lambda \frac{4I'_{b,\lambda}}{\omega_c}\operatorname{atan}\left(\frac{\omega_c}{\overline{\kappa}_\lambda}\right)d\lambda. \tag{62}$$

Eq. (62) provides a mathematical framework to define a new spectral averaging which results in a mean absorption coefficient that controls TRI. The new turbulence mean absorption coefficient can be calculated, in a first approximation, by dropping the averages and primes. By performing this procedure it is assumed that κ'_λ and κ'_p are negligible, which has been already substantiated, and that the ratio of the fluctuation of blackbody intensity to the mean is independent of wavelength ($I'_{b,\lambda}/I_{b,\lambda}(T) \neq f(\lambda)$)

$$\frac{\kappa_g(T)}{\omega_c}\operatorname{atan}\frac{\omega_c}{\kappa_g(T)} \equiv \frac{1}{\kappa_p(T) I_b(T)}\int_0^\infty \kappa^2_\lambda(T)\frac{I_{b,\lambda}(T)}{\omega_c}\operatorname{atan}\left(\frac{\omega_c}{\kappa_\lambda(T)}\right)d\lambda, \tag{63}$$

For simplicity, $\overline{\kappa}$ in Eq. (49) for the calculation of ω_c is substituted with $\overline{\kappa}_p$ both on the LHS and RHS of Eq. (63). The newly defined κ_g can be used to substitute κ_p in the coupling function f_G, such that the linear relation between G_{rms} and θ_{rms} can be written as

$$G^{\star}_{rms}(\kappa_g) = \frac{f_E \cdot \kappa_g(\overline{T}) + f_{\kappa_g}(\overline{E} - \overline{G})}{\omega_c}\operatorname{atan}\left(\frac{\omega_c}{\kappa_g(\overline{T})}\right)\cdot \theta_{rms}. \tag{64}$$

Fig. 16 shows profiles of κ_g compared to κ_p as functions of temperature and the respective G_{rms} profiles, both obtained from DNS and predicted by κ_p and κ_g. From top to bottom, Fig. 16 displays profiles for case H, C, and P, respectively. For all non-gray gas cases, using κ_g in the definition of f_G, leads to an accurate prediction of incident radiation fluctuations. Contrarily, employing κ_p always results in an under-prediction of G'. In particular, the disagreement is lowest for case P and the largest for case C. This discrepancy can be related to the difference between κ_g and κ_p. While for case P, $\kappa_g < 1.4\kappa_p$, for case H, $1.45\kappa_p < \kappa_g < 2\kappa_p$ and for case C $3\kappa_p < \kappa_g < 8\kappa_p$. As can be noted, for all the cases considered herein $\kappa_g > \kappa_p$. Yet, there is no proof to claim that this must be always the case. Nevertheless, it is apparent that the difference is related to the variability of the absorption spectrum. For example, if the absorption coefficient is independent of the wavelength (i.e., gray gas), then $\kappa_g = \kappa_p$. On the other hand, if the absorption coefficient shows a large variability, the weighting function $(\kappa_\lambda/\omega_c)\operatorname{atan}(\omega_c/\kappa_\lambda)$ within the integrand in Eq. (63) filters out the lowest, while retaining the largest spectral absorption coefficients. In other words, only the spectral lines with a large enough absorption coefficient will produce a noticeable G'_λ and contribute to the integrated effect.

Based on this analysis, it is now possible to define a new effective optical thickness τ_g by spatially averaging κ_g in wall-normal direction, as follows

$$\tau_g = \frac{1}{2}\int_0^2 \kappa_g(\overline{T})dy. \tag{65}$$

The obtained values of τ_g compared to τ are summarized for the non-gray gas cases in Table 3. In contrast to τ, the new parameter

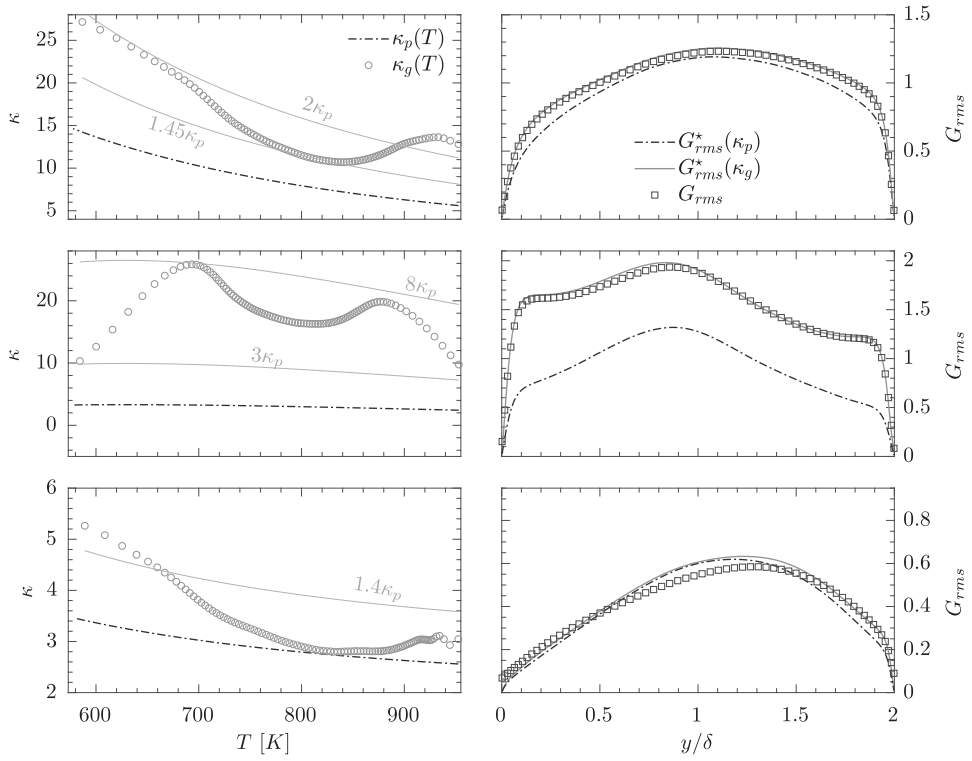

Fig. 16. Left: Planck mean absorption coefficient and turbulence mean absorption coefficient for cases H (top), C (center) and P (bottom) as a function of the temperature. These profiles are contingent to a turbulent fully developed channel flow. Lines of constant multiples of κ_p are added as a reference in gray. Right: Comparison between G_{rms} obtained by DNS (symbols) and $G^\star_{rms}$ obtained from Eqs. (44) and (64) for cases H (top), C (center) and P (bottom).

Table 3
Comparison between τ and τ_g.

Case	H	C	P
τ	8.02	2.99	2.79
τ_g	13.4	18.9	3.1

for the optical thickness τ_g is able to characterize TRI. Based on τ_g, case C has the highest optical thickness, followed by case H and P, consistent with what has been observed in the DNS results. It is possible to conclude, that κ_g is not only a convenient quantity useful to predict the fluctuations of incident radiation but also the parameter which unambiguously characterizes TRI in a non-gray turbulent flow.

Hereafter we provide a physical interpretation for the reason why τ_g is able to properly characterize TRI, where the other spectrally integrated parameters fail. The spectral transmissivity t_λ and normalized emission i_λ are defined as

$$t_\lambda = e^{-\kappa_\lambda} \qquad i_\lambda = \frac{\kappa_\lambda I_{b,\lambda}}{\max(\kappa_\lambda I_{b,\lambda})}. \tag{66}$$

While t_λ is a measure of absorption and, if integrated, leads to the global transmissivity t, i_λ shows the redistribution of emission over the wavelength and forms the basis τ's definition.

The comparison between cases P and C, shown in Fig. 17, displays quite effectively why neither τ or t can be used for characterizing TRI. If the t_λ is considered, case P appears the optically thickest case ($t = 0.10$ see Table 2), while case C, due to the limited width of the absorption bands is in average relatively transparent ($t = 0.88$). If the combination of t_λ and i_λ is taken into account on a spectral basis, it is possible to show why τ and t fail. While i_λ is significant throughout the whole spectrum for case P, for case C the emission is confined in regions where $t_\lambda \to 0$ resulting in an optically thick behaviour. It is not possible to categorize TRI if one of the two effects is neglected (i.e., using τ or t) since TRI is driven by the dual effect of emission and absorption on a spectral basis. On the other hand, deriving the definition of a new parameter based on G', as done in Eq. (63), allows to take into account the dual effect of spectral emission and absorption, since G' is necessarily produced by local E', see Eq. (42). The connection of i_λ and t_λ on a λ basis is intrinsically included in the definition of τ_g which is, therefore, the appropriate parameter to characterize TRI.

9. TRI correlations

Classically, TRI has been studied with the use of correlations that describe the influence of radiative field fluctuations. In particular, the focus has always been on identifying the deviation of the radiative heat source from the one obtained by mean quantities. This corresponds to investigating the $\kappa', E', G' \to \overline{\theta}$ path in Fig. 1. The definition of TRI correlations follows from the averaging of Eq. (8)

$$\overline{Q}_r = \overline{\kappa}_p \overline{E} - \overline{\kappa}_p \overline{G} + \underbrace{\overline{\kappa'_p E'}}_{\text{emission TRI}} - \underbrace{\overline{\kappa'_p G'}}_{\text{absorption TRI}} \tag{67}$$

where the last two terms are the TRI contributions divided into emission and absorption TRI. The correlations, relate the magnitude of the TRI terms to the averaged terms, as done in [4]

$$R_{\kappa E} \equiv -\frac{\overline{\kappa'_p E'}}{\overline{\kappa}_p \overline{E}} \quad R_{\kappa G} \equiv -\frac{\overline{\kappa'_p G'}}{\overline{\kappa}_p \overline{G}}. \tag{68}$$

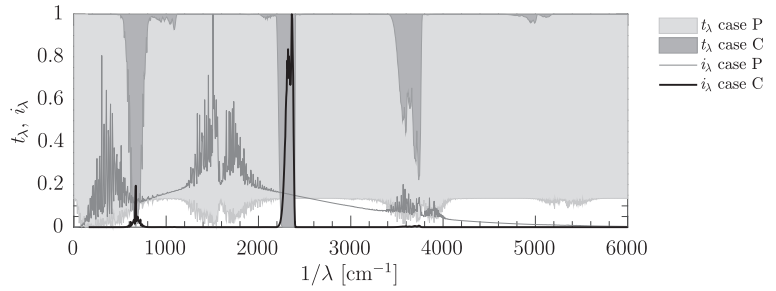

Fig. 17. Spectral transmissivity and normalized emission for non-gray cases P and C at 800 [K].

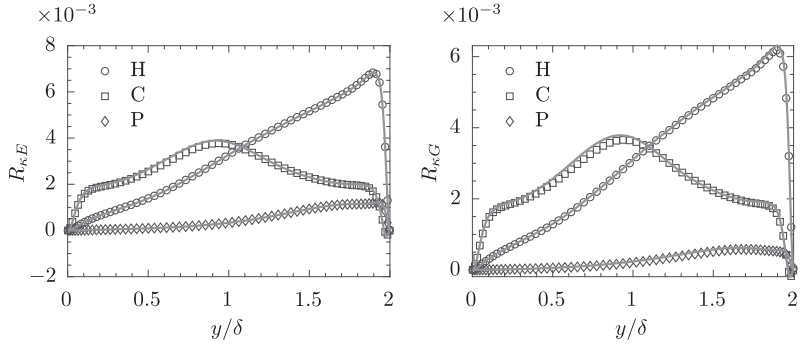

Fig. 18. TRI correlation and their models for the non-gray cases. Symbols: DNS results ($R_{\kappa E}$ and $R_{\kappa G}$). Lines: modeled terms ($R^\star_{\kappa E}$ and $R^\star_{\kappa G}$).

These can be estimated using temperature variance as

$$R^\star_{\kappa E} = -\frac{f_\kappa f_E}{\overline{\kappa}_p \overline{E}}\overline{\theta'^2} \quad R^\star_{\kappa G} = -\frac{f_\kappa f_G}{\overline{\kappa}_p \overline{G}}\overline{\theta'^2}. \tag{69}$$

Fig. 18 shows the above defined TRI correlations obtained by DNS, compared to the modeled terms showing an excellent agreement. Notice that, indeed, the magnitude of the correlations is relatively low $O(10^{-3})$ confirming that the direct influence of radiative fluctuations on the mean temperature is negligible in non-reactive turbulent flows.

10. Summary and concluding remarks

In the present work, we performed a comprehensive study to quantify the effect of κ on TRI in a turbulent channel flow of an absorbing, emitting participating media. The analysis has been realized with the aid of DNS of a gray gas with $\kappa = f(T)$ and a non-gray gas with different absorption spectra. We analytically derive relations that express radiative field fluctuations as linear functions of temperature fluctuations. The assumptions employed have been critically assessed by comparing the predictions with DNS showing an excellent accuracy. These derivations allowed to identify the impact of $\overline{\kappa}$ and κ' on the modification of the temperature field. Investigating the gray gas results, it was demonstrated that TRI, in the investigated cases, is fully accounted for by the variations of the mean absorption coefficient alone. For all purposes, in a non-reactive turbulent flow, κ' can be neglected, independently from the value of τ.

Moreover, we defined a diagnostic quantity $\mathcal{A}_{\overline{\kappa}}/(\mathcal{E}_{\overline{\kappa}} - \mathcal{A}_{\overline{\kappa}})$ that allows a monotonic comparison between TRI for flows of different τ values. With this quantity, the influence of TRI for three different non-gray gas cases was assessed. The results show that the behaviour of a non-gray gas is decoupled from the value of the Planck-mean optical thickness. In particular, the variability of the absorption spectrum impacts the interactions between temperature and radiative field. Therefore, from the approximation of incident radiation fluctuations (which are responsible for the behavioural changes in TRI effects), a new definition of spectrally averaged absorption coefficient has been derived. This new turbulence based mean absorption coefficient κ_g proves to effectively predict TRI in non-gray gas turbulent flows. In addition, κ_g provides the base for the definition of a new optical thickness τ_g which allows a conclusive comparison among gray and non-gray cases.

Appendix A. Incident radiation turbulent spectrum

The derivations performed in Section 4.3 rely on a Fourier transformation of the incident radiation. In doing so, the modes of G are related to the E and κ modes. It is necessary, therefore, to verify if the derivations hold in a Fourier transformed domain, before the inverse Fourier transform, Eq. (42), is performed. From Eq. (41), by neglecting the influence of absorption coefficient modes, we obtain

$$\widehat{G}' \approx \left(\frac{\overline{\kappa}}{\omega_c}\operatorname{atan}\frac{\omega_c}{\overline{\kappa}}\right)\cdot \widehat{E}'. \tag{A.1}$$

Due to the considerations performed in Section 8.2, in case of a non-gray gas, the $\overline{\kappa}$ in Eq. (A.1) is substituted with κ_g. The approximation of the incident radiation turbulent spectrum follows

$$\mathcal{S}_G \approx \mathcal{S}^\star_G = \left(\frac{\overline{\kappa}}{\omega_c}\operatorname{atan}\frac{\omega_c}{\overline{\kappa}}\right)^2 \cdot \mathcal{S}_E, \tag{A.2}$$

where $\mathcal{S}^\star_G$ is the model for the incident radiation spectra. Eq. (A.2) entails that the shape of $\mathcal{S}_G$ is the same as for the E spectrum. This is not necessarily true, but it is a more appropriate approximation as τ (or τ_g for non-gray gas) grows.

On the other hand, a relevant level of G' is found only at high τ. In general, as the G spectrum increases in value, it approaches $\mathcal{S}_E$, which is the limit in the case τ (or τ_g for non-gray gases) $\to \infty$. Fig. A.1 shows the streamwise pre-multiplied turbulent incident radiation spectrum for the different cases, in the center of the channel ($y/\delta = 1$) and near the wall ($y/\delta = 1.93$). Fig. A.1 proves that the incident radiation spectrum, in these cases, can be approximated using the turbulent emission spectrum.

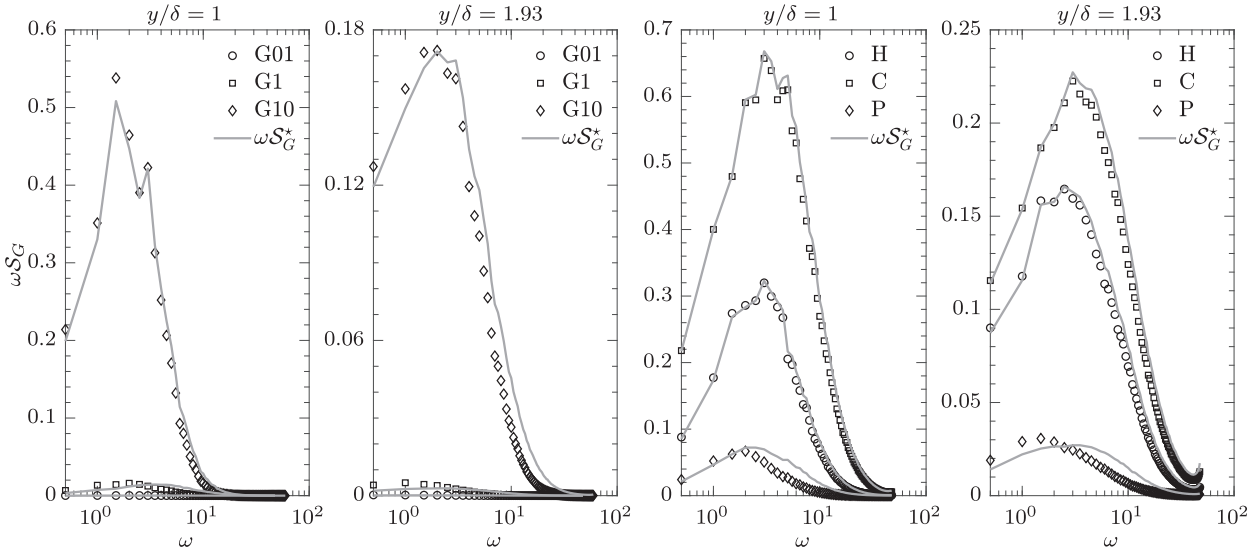

Fig. A.1. Profiles of streamwise pre-multiplied incident radiation spectra for the different cases. Symbols represent DNS obtained profiles, lines show the $\mathcal{S}_G$ approximated with formula (A.2).

References

[1] Coelho P. Turbulence radiation interaction: from theory to application in numerical simulations. J Heat Transf 2012;134.

[2] Coelho P, Teerling O, Roekaerts D. Spectral radiative effects and turbulence/radiation interaction in a non-luminous turbulent jet diffusion flame. Combust Flame 2003;133:75–91.

[3] Gupta A, Modest M, Haworth D. Large-eddy simulation of turbulence-radiation interactions in a turbulent planar channel flow. J Heat Transf 2009;131(6). doi:10.1115/1.3085875.

[4] Deshmukh K, Modest M, Haworth D. Direct numerical simulation of turbulence-radiation interactions in a statistically one-dimensional nonpremixed system. J Quant Spectrosc Radiat Transf 2008;109:2391–400.

[5] Tesse L, Dupoirieux F, Taine J. Monte Carlo modeling of radiative transfer in a turbulent sooty flame. Int J Heat Mass Transf 2004;47:555–72.

[6] Roger M, Coelho P, Silva CD. Relevance of the subgrid-scales for large eddy simulations of turbulence-radiation interactions in a turbulent plane jet. J Quant Spectrosc Radiat Transf 2011;112:1250–6.

[7] Sakurai A, Matsubara K, Takakuwa K, Kanbayashi R. Radiation effects on mixed turbulent natural and forced convection in a horizontal channel using direct numerical simulation. Int J Heat Mass Transf 2010;55:2539–48. doi:10.1016/j.ijheatmasstransfer.2012.01.006.

[8] Vicquelin R, Zhang Y, Gicquel O, Taine J. Effects of radiation in turbulent channel flow: analysis of coupled direct numerical simulations. J Fluid Mech 2014;753:360–401. doi:10.1017/jfm.2014.368.

[9] Zhang Y, Vicquelin R, Gicquel O, Taine J. Physical study of radiation effects on the boundary layer structure in a turbulent channel flow. Int J Heat Mass Transf 2013;61:654–66.

[10] Ghosh S, Friedrich R, Stemmer C. Contrasting turbulence-radiation interaction in supersonic channel and pipe flow. Int J Heat Fluid Flow 2014;48:24–34. doi:10.1016/j.ijheatfluidflow.2014.04.002.

[11] Ghosh S, Friedrich R. Effects of radiative heat transfer on the turbulence structure in inert and reacting mixing layers. Phys Fluids 2015;27. doi:10.1063/1.4920990.

[12] Silvestri S, Patel A, Roekaerts D, Pecnik R. Turbulence radiation interaction in channel flow with various optical depths. J Fluid Mech 2018;834:359–84.

[13] Grosshandler W. RADCAL: a narrow-band model for radiation calculations in a combustion environment. Technical Report. NIST technical note; 1993.

[14] Soufiani A. Temperature turbulence spectrum for high-temperature radiating gases. J Thermophys 1991;5:489–94.

[15] Patel A, Peeters J, Boersma B, Pecnik R. Semi-local scaling and turbulence modulation in variable property turbulent channel flows. Phys Fluids 2015;27(7). doi:10.1063/1.4929813.

[16] Boersma B. A 6th order staggered compact finite difference method for the incompressible Navier Stokes and scalar transport equations. J Comput Phys 2011;230:4940–54.

[17] Lele S. Compact finite difference schemes with spectral-like resolution. J Comput Phys 1992;103:16–42.

[18] Chai J, Lee H, Patankar S. Finite volume method for radiation heat transfer. J Thermophys Heat Transf 1994;8(3):419–25.

[19] Coelho P. Bounded skew high-order resolution schemes for the discrete ordinates method. J Comput Phys 2002;175:412–37. doi:10.1006/jcph.2001.6899.

[20] Zhang Y, Gicquel O, Taine J. Optimized emission-based reciprocity monte carlo method to speed up computation in complex systems. Int J Heat Mass Transf 2012;55:8172–7.

[21] Rothman L. The HITRAN2012 molecular spectroscopic database. J Quant Spectrosc Radiat Transf 2013;130:4–50.

[22] Silvestri S, Pecnik R. A fast GPU Monte Carlo radiative heat transfer implementation for coupling with direct numerical simulation. J Comput Phys 2019;100032. doi:10.1016/j.jcpx.2019.100032.